Semnan University

Progress in Physics of Applied Materials

journal homepage: https://ppam.semnan.ac.ir/

Influence of bismuth substitution on structural and optical properties of $CuFe_{2-x}Bi_xO_4$ spinel structure

Hamid Hamrah, Ahmad Gholizadeh*

School of Physics, Damghan University, Damghan, Iran

ARTICLE INFO

Article history:
Received: 22 August 2024
Revised: 01 September 2024
Accepted: 01 October 2024

Keywords:
Copper spinel ferrite
Bismuth substitution
Structural properties
Phase transition
Optical band gap energy

ABSTRACT

$CuFe_{2-x}Bi_xO_4$ (x=0.0-2.0) spinel structures were synthesized using a sol-gel auto-combustion method. The effects of Bi^{3+} substitution on structural and optical properties were investigated using X-ray diffraction, Fourier-transformed infrared spectroscopy, and UV-Vis spectroscopy. A phase transition was observed in $CuFe_{2-x}Bi_xO_4$ with increasing Bi content, leading to enhanced lattice parameters a and c due to Bi^{3+} larger ionic radius. As Bi substitution increased, the crystallite size decreased due to the reduced mobility and higher mass of Bi^{3+} ions. Controlled Bi substitution achieved the tunability of structural and optical properties, while local distortions from Bi^{3+} ions in the $CuFe_2O_4$ lattice increased the optical band gap energy. $CuFe_{2-x}Bi_xO_4$ spinel structures show promise for applications in photocatalysis, gas sensors, pigments, and magnetic materials. We will clearly explain what we already know about Bi^{3+}-substituted copper ferrite nanoparticles and stress how important it is to fully understand the changes in structure and optical properties that happen when Bi^{3+} is added.

1. Introduction

Many modern technological devices are related to magnetic materials. These devices include electric generators, transformers, electric motors, computers, and more. Ferrites are ceramic materials made from a mixture of iron oxide and divalent metals like barium, strontium, cerium, nickel, cobalt, and more. Ferrites are hard and brittle with a gray or black color, and they are part of a special group of materials called ferrimagnetic materials. Natural magnetite, or magnetite with the chemical formula Fe_3O4, is an example of a ferrite that has been used for centuries to make compasses. Ferrites are not very strong, but they are widely used in various industries due to their unique properties, such as their low cost and versatility. Ferrites have made significant progress in the fields of electronics and communications in recent years. Their thermal stability, electrical conductivity, electrocatalytic activity, and structural resistance are far superior to other structures [1]. They are widely used in computer peripherals, telecommunications equipment, permanent magnets, electronic devices, and microwave ovens [2]. These materials are also important from a technological perspective and have been used in many applications, including magnetic recording and coating media for information storage or retrieval, magnetic resonance imaging (MRI), catalysts, sensors, pigments, and others [3,4]. In addition, the properties of ferrites are heavily dependent on their size and shape [5-7].

Spinel ferrite is a magnetic substance with a spinel structure, having a chemical formula of $CuFe_2O_4$. There have been extensive studies on pure $CuFe_2O_4$, and its synthesis via electrochemical [8] and ceramic [9,10] methods have been reported [11]. Furthermore, $CuFe_2O_4$ is of significant importance for the completion of O2 from the alumina-cryolite system, which is used in aluminum

* Corresponding author. Tel.: +989120816781
E-mail address: gholizadeh@du.ac.ir (A. Gholizadeh).

Cite this article as: Cite this article as: Hamrah H., Gholizadeh A., 2024. Influence of bismuth substitution on structural and optical properties of $CuFe_{2-x}Bi_xO_4$ spinel structure. *Progress in Physics of Applied Materials, 4*(2), pp. DOI: 10.22075/ppam.2024.35097.1113

production, due to its high electronic conductivity, high thermal stability, and high catalytic activity. Its importance lies in its function as a non-consumable and green anode for aluminum electrolysis, where only oxygen gas is generated instead of CO_2. The distribution of cations in ferrite spinel can be represented by the following formula: $(Cu_{\delta}^{2+}Fe_{1-\delta}^{3+})_A[Cu_{1-\delta}^{2+}Fe_{1+\delta}^{3+}]_B$, where δ is the cation distribution ratio. For δ = 1, it shows the tetragonal phase, whereas, for δ = 0, it shows the cubic phase. The tetragonal structure with space group $I4_1/amd$ is stable in $CuFe_2O_4$ compositions above 663 K, while the cubic structure with space group $Fd\bar{3}m$ exhibits lower temperatures [12].

Ferrite spinel is an important material due to its strong applications in magnetic memory, high-frequency devices, resonators, drug delivery, and high-quality filters for high-speed digital data storage [13,14]. Additionally, it demonstrates a desirable catalytic performance in hydrogen production and the removal of aluminum alloys. Nanocrystalline ferrites have been extensively studied for their potential applications in non-destructive testing equipment, radio frequency coils, antenna devices, high-quality filters, and read/write heads for high-speed digital data storage [15,16].

In this work, the $CuFe_{2-x}Bi_xO_4$ spinel oxides prepared using the citrate-nitrate method were characterized using several techniques. The goal of synthesizing these compounds is to examine the effects of bismuth substitution for iron at tetrahedral and octahedral sites through structural and optical studies, which was not reported so far. We will clearly outline the existing knowledge in the field of Bi^{3+}-substituted copper ferrite nanoparticles, focusing on the need for a comprehensive understanding of the structural and optical property changes resulting from Bi^{3+} substitution. This will help highlight the gap in the current literature that our study aims to fill. We will explicitly state the primary objectives of our research, ensuring that they are concise and easily identifiable. These objectives will focus on investigating the effects of Bi^{3+} substitution on particle size, lattice parameter, and optical bandgap energy, as well as understanding the underlying mechanisms responsible for these changes.

2. Experimental

$CuFe_{2-x}Bi_xO_4$ (x=0.0, 0.2, 0.4, 0.6, 0.8, 1.2, 1.6, and 2.0) samples were synthesized using the citrate-nitrate method, as described in references [17-19]. High-purity metal nitrate salts (Merck) and citric acid ($C_7O_8H_6$) were employed in the process. The appropriate quantities of metal nitrates ($Fe(NO_3)_3.9H_2O$, and $Cu(NO_3)_3.6H_2O$) and citric acid (1:1 ratio) were dissolved separately in deionized water with the assistance of a magnetic stirrer. Bismuth nitrate ($Bi(NO_3)_2.5H_2O$) was dissolved in a minimal amount of nitric acid and then combined with the other solutions. The final solution was stirred for at least 1 h to achieve a clear and homogeneous mixture, followed by placing it in a water bath at approximately 80 °C until a dry gel formed. The dried gel was heated in an oven at 200 °C for 10 h. The obtained powders were then calcined at 750 °C for 2 h to obtain the spinel structure. Names of the samples were abbreviated in Table 1.

Powder X-ray diffraction (XRD) patterns of the samples were analyzed using a Bruker AXS-D8 XRD machine featuring a Cu-Kα source (30 kV and 35 mA) and a nickel filter. The XRD analysis was conducted in the 2θ range of 10-80° with a step size of 0.05° and a wavelength of 1.5404 Å. Fourier-transform infrared (FT-IR) spectra were measured within the 400-1900 cm-1 spectral range using a Perkin-Elmer RXI FT-IR spectrometer. The samples were mixed with KBr and pressed into pellets using a press machine with a pressure of 10 tons for FT-IR analysis. Ultraviolet-visible (UV-Vis) spectra were recorded in a wavelength range of 200–1100 nm using a UNICO SQ-4802 UV–Vis double-beam spectrophotometer to evaluate the optical band gap energy of the samples. The optical band gap energy of all the samples was calculated using the classical Tauc relation [20]:

$$(\alpha h\upsilon)^2 = A(h\upsilon - E_g) \quad (1)$$

Where A, hυ, and E_g are constants, photon energy, and optical band gap energy, respectively. The direct bandgap energies of $CuFe_{2-x}Bi_xO_4$ (x=0.0, 0.2, 0.4, 0.6, 0.8, 1.2, 1.6, and 2.0) were determined by plotting $(\alpha h\upsilon)^2$ versus the hυ. The use of the exponent 2 in the Tauc relation, $(\alpha h\upsilon)^2$, is based on the assumption that the absorption coefficient (α) is related to the photon energy (hυ) through a power-law dependence for direct bandgap materials. The exponent value of 2 corresponds to the case of direct bandgap transitions in semiconductors, which involve the direct recombination of electrons and holes without the need for phonon-assisted processes. The Tauc relation provides a simple and widely used method for estimating the direct bandgap energies of semiconductor materials. While it does not explicitly account for the wave number dependence of the dipole dielectric matrix, it is still an effective tool for analyzing the bandgap energies and optical properties of materials, as demonstrated in our study.

3. Results and discussion

3.1 Structural properties

The XRD patterns for CuFe2-xBixO4 (x=0.0, 0.2, 0.4, 0.6, 0.8, 1.2, 1.6, and 2.0) are presented in Fig. 1. Structural analysis of the samples was carried out using the X'Pert software package. Structural analysis reveals that the dominant phase of the x=0.0, 0.2 samples have a tetragonal structure with space group $I4_1/amd$, matching the standard ICDD card No. 00-034-0425 [21,22]. However, for samples with higher Bi content (x = 0.4, 0.6, 0.8, 1.2, 1.6, and 2.0), the dominant phase exhibits a tetragonal structure with space group $P\bar{4}ncc$, corresponding to the standard JPCDS card No. 01-080-1908 [23-27]. A structural phase transition from tetragonal space group $I4_1/amd$ to $P\bar{4}ncc$ was observed with increasing Bi content. Impurity phases of CuO and BiFeO3 were detected in samples with 0.2≤x≤1.6 as

labeled on Fig. 1. The crystal structure of $CuFe_2O_4$ can be cubic or tetragonal, depending on Cu^{2+} ion concentration and thermal conditions [14,21]. In $CuFe_2O_4$, Cu2+ ions primarily occupy octahedral sites. As Bi^{3+} replaces Fe3+, the larger Bi^{3+} ions force Cu^{2+} ions to transfer from octahedral to tetrahedral sites. This reduces Jahn-Teller distortion and results in a phase transition. With increasing Bi concentration, the intensity of the BiFeO3 secondary phase also increases due to excess Bi^{3+} ions forming impure phases. Peak shifts in the XRD patterns indicate an increase in the unit cell volume of the tetragonal structure due to the larger ionic radius of Bi^{3+} compared to Fe3+. As listed in Table 1, with increasing Bi content in $CuFe_2O_4$, both lattice parameters a and c of the tetragonal phase tend to increase. This observation can be attributed to the larger ionic radius of Bi^{3+} compared to the ions it replaces in the $CuFe_2O_4$ lattice, causing an expansion in the unit cell volume. The increase in lattice parameters indicates a significant influence of Bi substitution on the structural properties of the $CuFe_2O_4$ material.

The Halder-Wagner (H-W) method was employed to extract data on crystallite size (D) and microstrain (ε) [19]:

$$\left(\frac{\beta^*_{hkl}}{d^*_{hkl}}\right)^2 = \left(\frac{\varepsilon}{2}\right)^2 + \left(\frac{\beta^*_{hkl}}{d^*_{hkl}{}^2}\right)\left(\frac{1}{D}\right) \qquad (2)$$

where $\frac{\beta_{hkl}\cos\theta}{\lambda} = \beta^*_{hkl}$ and $\frac{2\sin\theta}{\lambda} = d^*_{hkl}$.

Halder-Wagner plots of $\left(\frac{\beta^*_{hkl}}{d^*_{hkl}}\right)^2$ versus $\left(\frac{\beta^*_{hkl}}{d^*_{hkl}{}^2}\right)$ are shown in Fig. 2. The Scherrer and Halder-Wagner methods yielded the results for crystallite size and microstrain of the samples, as shown in Table 1. According to the values presented in this table, the crystallite size decreases with increasing substitution, as determined by the Scherrer method. Calculations using the Halder-Wagner method also resulted in values similar to those obtained by the Scherrer method, demonstrating a decrease in crystallite size with increased substitution. The decrease in crystallite size with higher Bi^{3+} ion substitution can be attributed to the heavier mass and reduced mobility of Bi^{3+} ions compared to Fe3+ ions [25,28]. This reduced mobility leads to a lower tendency for the formation of larger crystallites during the synthesis process. Moreover, changes in microstrain can be associated with variations in defect and dislocation densities, particularly those related to impurity phases [28,29].

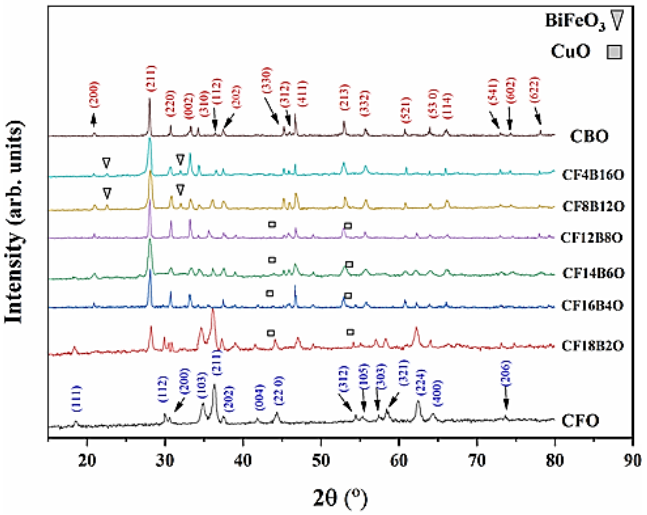

Fig. 1. The XRD patterns of $CuFe_{2-x}Bi_xO_4$.

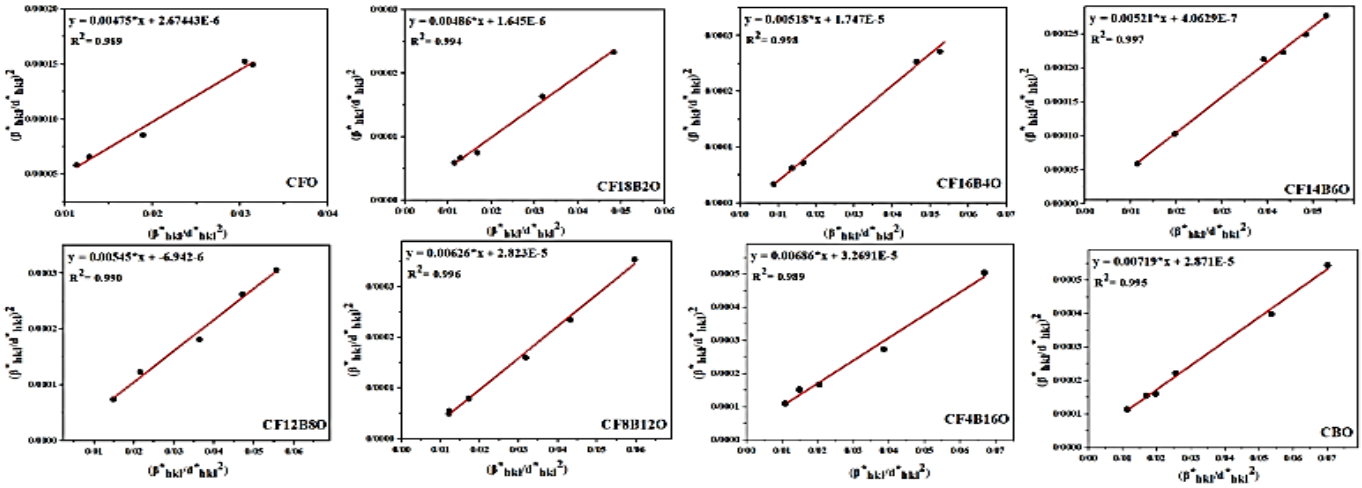

Fig. 2. Halder-Wagner plots for $CuFe_{2-x}Bi_xO_4$.

Table 1. Crystallite sizes, as determined by the Scherrer (D_{Sch}), and Hälder-Wagner ($D_{H\text{-}W}$) and microstrain along with the lattice parameter values of $CuFe_{2-x}Bi_xO_4$.

Sample	Abbreviation	Crystallite size		Microstrain × 10^3 unitless	Lattice parameters (Å)	
		D_{Sch}	$D_{H\text{-}W}$	ε	a	c
x = 0.0	CFO	18.82	21.05	3.65	5.785	8.549
x = 0.2	CF18B2O	18.25	20.59	2.57	5.801	8.858
x = 0.4	CF16B4O	18.19	19.30	4.50	8.517	5.848
x = 0.6	CF14B6O	17.97	19.23	1.27	8.495	5.832
x = 0.8	CF12B8O	17.10	18.348	5.27	8.497	5.847
x = 1.2	CF8B12O	15.84	15.97	10.63	8.471	5.827
x = 1.6	CF4B16O	14.40	14.57	12.21	8.317	6.397
x = 2.0	CBO	13.58	14.04	3.42	8.508	5.843

3.2 FTIR spectra

FTIR absorption peaks are related to the lattice vibrations of metal ions in the spinel network. The spinel structure has two distinct absorption peaks corresponding to the tetrahedral and octahedral sites at wavenumbers lower than 800 cm^{-1}. Higher wavenumber peaks (ν_1) are associated with the metal-oxygen lattice vibrations at the tetrahedral site, while lower wavenumber peaks (ν_2) are related to the metal-oxygen lattice vibrations at the octahedral site. The difference in wavenumber (ν_1) and (ν_2) is associated with the shorter bond length of the metal-oxygen ions at the tetrahedral sites and the longer bond length of the metal-oxygen ions at the octahedral sites, as well as the respective ion charges. The FTIR absorption spectra related to the stretching vibrations of metal ions in the spinel lattice are shown in Fig. 3(a) for the $CuFe_{2-x}Bi_xO_4$. The absorption peaks related to the tetrahedral site are in the range of 527-610 cm^{-1}, and for the octahedral site, they are in the range of 414-430 cm^{-1} [21,22, 26]. It is observed that with increasing Bi substitution, the absorption peaks shift towards lower wavenumbers. Also, it is observed that the ν_2 peak does not exist for the $CuBi_2O_4$ sample Due to the limitations in measuring below 400 cm^{-1}. To explain the reason for this change in the absorption peak, we first refer to the simplified theoretical explanation for stretching vibrations [26].

The characteristics of a stretching vibration can be studied using a mechanical model called the harmonic oscillator. A harmonic oscillator consists of two masses connected by a spring and undergoing simple harmonic motion (motion on a plane without friction while one side is fixed) along the axis of the spring (see Fig. 3(b)). If the system is displaced by a distance x from its equilibrium position (Re) and then released, it will begin to oscillate. The period of this oscillation depends on the spring force constant (K) and the masses. It should be noted that for a real bond, the spring force constant is a measure of the bond's hardness and stiffness.

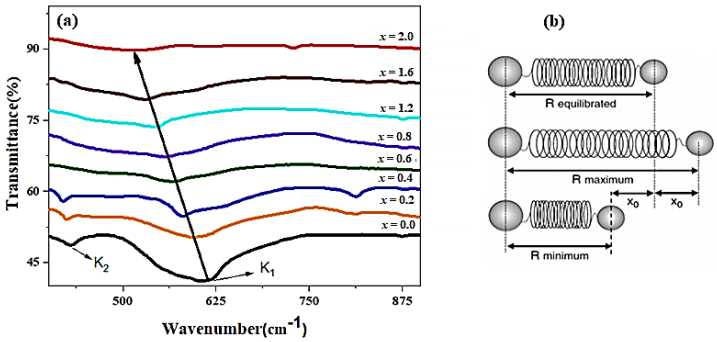

Fig. 3 (a) FTIR spectra of $CuFe_{2-x}Bi_xO_4$, (b) a molecular (spring-mass) system consisting of two atoms that form a harmonic oscillator.

Motion frequency (ν) is independent of the x_o and is obtained using Hooke's Law: $\nu = \frac{1}{2\pi}\sqrt{\frac{k}{\mu}}$, where μ denotes the reduced mass in kg for a two-component system, equivalent to $\mu = \frac{1}{\frac{1}{m_1}+\frac{1}{m_2}} = \frac{m_1 m_2}{m_1+m_2}$. In an ideal situation, for a tetrahedral site, m_1 corresponds to the mass of oxygen and m_2 corresponds to the average mass of iron and copper, and for an octahedral site, m_1 denotes the mass of oxygen and m_2 represents the average mass of iron and bismuth. If we define the wave number $\bar{k}$ as follows: $\bar{k} = \frac{1}{\lambda} = \frac{\nu}{c}$; So, $\bar{k} = \frac{1}{2\pi c}\sqrt{\frac{K}{\mu}}$.

Now, considering the above equations, we realize that if the mass m_2 increases or decreases, the reduced mass μ also decreases or increases, respectively. On the other hand, the wave number $\bar{k}$ is inversely proportional to the reduced mass μ, meaning that with a decrease or increase in the reduced mass μ, the wave number $\bar{k}$ will increase or decrease, respectively. As it is evident, the mass of bismuth is greater than that of iron; therefore, in the octahedral site, the reduced mass μ increases when bismuth substitutes for iron, which consequently leads to a shift of the absorption band ν_2, related to the octahedral site, towards the smaller wavenumber region. The positions of the absorption bands (k_1) and (k_2) are listed in Table 2. Referring to Fig. 3 and Table 2, in the $CuFe_2O_4$

sample, both bands k_1 and k_2 are observed, but only the band k_1 is observed in the CuBi2O4 sample [24, 26]. This is due to the longer bond length of Bi^{3+}-O^{2-} compared to Fe^{3+}-O^{2-}, as well as its higher mass. The absorption band ν_2, related to the octahedral site, shifts towards smaller wavenumbers with the substitution of bismuth for iron, and it is observed that this band appears at 430 cm^{-1} for the $CuFe_2O_4$ sample, but it does not exist in the $CuBi_2O_4$ sample.

Table 2. Positions of the absorption bands for $CuFe_{2-x}Bi_xO_4$.

Sample	x = 0.0	x = 0.2	x = 0.4	x = 0.6	x = 0.8	x = 1.2	x = 1.6	x = 2.0
$\bar{k}_2$ (cm^{-1})	430	421	414	---	---	---	---	---
$\bar{k}_1$ (cm^{-1})	610	590	581	568	559	547	538	527

3.3 Optical properties

Fig. 4 illustrates the $(\alpha h\upsilon)^2$ plots for all samples to obtain their energy gap. The resulting linear extrapolations from the plots are listed in Fig. 4 to calculate the energy gaps of the samples and are listed in Table 3. According to Table 3, it is evident that increasing the Bi substitution level results in an increased energy gap for the samples. The increase in optical band gap energy could be attributed to the following factors [28,29]:

Changes in crystal structure: The introduction of Bi into the $CuFe_2O_4$ lattice may cause local distortions, which could lead to the crystal structure transition from a tetragonal structure with space group $I4_1/amd$, to another tetragonal structure with space group $P\bar{4}ncc$ as reported in our structural analysis [28]. These structural changes due to higher bond length Bi-O than Fe-O might result in an increase in the optical band gap energy due to modifications in the electronic structure and chemical bonding. On the other words, $CuBi_2O_4$ has higher optical band gap energy than $CuFe_2O_4$.

Burstein-Moss effect: The Burstein-Moss effect occurs when the doping concentration is high enough to cause the Fermi level to move closer to the conduction band [20]. This leads to an increase in the apparent optical band gap energy due to the occupation of the lower energy levels in the conduction band by electrons.

Phase separation: In some cases, high Bi substitution might lead to phase separation or the formation of secondary phases, which could have different electronic properties and bandgap energies [29]. If these secondary phases have higher optical band gap energy, it could result in an overall increase in the observed optical band gap energy.

Also, such behavior of the measured band gap (E_g^*) may be explained based on Brass's effective mass model [29], which can be expressed as a function of crystallite size:

$$E_g^* = E_g^{bulk} + \frac{h^2}{8er^2}\left(\frac{1}{m_e} + \frac{1}{m_h}\right) - \frac{1.8\,e^2}{4\pi\varepsilon_o\,\varepsilon\,r} \qquad (3)$$

where E_g^{bulk}, m_e, r, and m_h are the bulk energy gap, the effective mass of electrons, the crystallite size, and the effective mass of holes, respectively. ε, ε_o, e, and h are the relative permittivity, the permittivity of free space, electron charge, and Planck constant. According to this model, the energy band gap increases as the crystallite size decreases with increasing Bi substitution.

It is important to keep in mind that adding Bi can change the optical band gap energy of $CuFe_{2-x}BixO_4$. These changes can be different depending on the synthesis conditions, the amount of Bi used, and the microstructure of the sample.

A detailed analysis of the material's structure, composition, and electronic properties is necessary to understand the underlying mechanisms responsible for any observed increase in optical band gap energy.

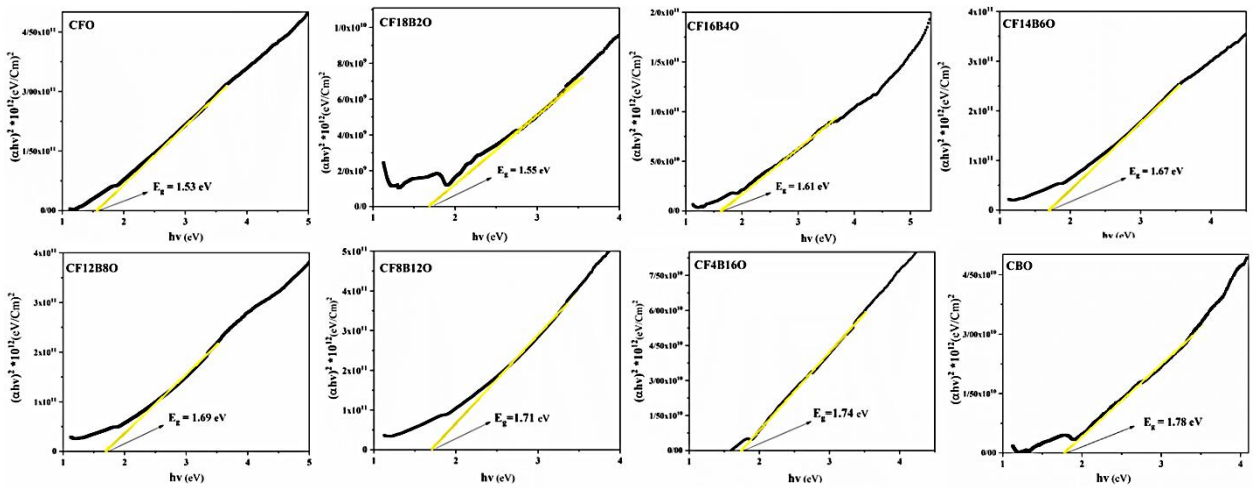

Fig. 4 $(\alpha h\upsilon)^2$ plots for $CuFe_{2-x}Bi_xO_4$ to determine their energy gaps.

Table 3. the calculated energy gap values for $CuFe_{2-x}Bi_xO_4$.

Sample	x = 0.0	x = 0.2	x = 0.4	x = 0.6	x = 0.8	x = 1.2	x = 1.6	x = 2.0
$Eg(eV)$	1.53	1.55	1.61	1.67	1.69	1.71	1.74	1.78

4. Conclusion

This research looks into what happens when bismuth is added to $CuFe_{2-x}Bi_xO_4$ spinel structures and how that changes their structure and optical properties

X-ray diffraction analysis reveals a phase transition from tetragonal space group $I4_1/amd$ to $P\bar{4}ncc$ with increasing Bi content. The lattice parameters a and c also increase due to the larger ionic radius of Bi^{3+} compared to Fe^{3+}. Crystallite size decreases with higher Bi substitution, which can be attributed to the heavier mass and reduced mobility of Bi^{3+} ions. Furthermore, changes in microstrain are associated with variations in defect and dislocation densities related to impurity phases. The influence of Bi substitution on the optical properties of $CuFe_{2-x}BixO_4$ is investigated through diffuse reflectance spectroscopy. The optical band gap energy demonstrates an increasing trend with Bi content, which may result from local distortions caused by the introduction of Bi^{3+} ions into the $CuFe_2O_4$ lattice. These structural changes can affect electronic structure and chemical bonding, leading to modifications in the optical band gap energy. This comprehensive analysis provides valuable insights into the tunability of the structural and optical properties of $CuFe_{2-x}Bi_xO_4$ spinel structures with controlled Bi substitution.

Acknowledgements

Conflicts of Interest

The author declares that there is no conflict of interest regarding the publication of this article.

References

[1] Laokul, P., Amornkitbamrung, V., Seraphin, S., and Maensiri, S., 2010. Characterization and magnetic properties of nanocrystalline CuFe2O4, NiFe2O4, ZnFe2O4 powders prepared by the Aloe vera extract solution. *Current Applied Physics*, 11(1), pp.101-108.

[2] Harris, V.G., Koon, N.C., Williams, C.M., Zhang, Q., Ab, M., and Kirkland, J.P., 1996. Cation distribution in NiZn-ferrite films via extended x-ray absorption fine structure. *Applied Physics Letters*, 68(15), p.2082.

[3] Satheeshkumar, M.K., Kumar, E.R., Srinivas, Ch., Prasad, G., Meena, S.S., Pradeep, I., Suriyanarayanan, N., and Sastry, D.L., 2014. Structural and magnetic properties of CuFe2O4 as-prepared and thermally treated spinel nanoferrites. *Indian Journal of Pure & Applied Physics*, 52, pp.124-130.

[4] Kalai Selvan, R., Augustin, C.O., Berchmans, L.J., and Saraswathi, R., 2003. Combustion synthesis of CuFe2O4. *Materials Research Bulletin*, 38, pp.41-54.

[5] Bahadur, D., 1992. Current trends in applications of magnetic ceramic materials. *Bulletin of Materials Science*, 15, pp.431-439."

[6] Sugimoto, M., 1999. The Past, Present, and Future of Ferrites. *American Ceramic Society*, 82(2), pp.269-280.

[7] Šafařík, I., and Šafaříková, 1992. Magnetic Nanoparticles and Biosciences. *Nanostructured Materials*, pp.1-23.

[8] Sartale, S.D., and Lokhande, C.D., 2001. Electrochemical deposition and oxidation of CuFe2 alloy: a new method to deposit CuFe2O4 thin films at room temperature. *Materials Chemistry and Physics*, 70(3), pp.274-284.

[9] Mazen, S., 2000. Tetravalent ions substitution in Cu – ferrite; structure formation and electrical properties. *Materials Chemistry and Physics*, 62(2), pp.131-138.

[10] Mahajan, R.P., Patankar, K.K., Kothale, M.B., and Patil, S.A., 2000. Conductivity, dielectric behaviour and magnetoelectric effect in copper ferrite-barium titanate composites. *Bulletin of Materials Science*, 23, pp.273-279.

[11] Pati, A.N., Mahajan, R.P., Patankar, K.K., Ghatage, A.K., Mathe, V.L., and Patil, S.A., 2000. Conduction mechanism in CuxFe3-xO4. *Indian Journal of Pure & Applied Physics*, pp.651-656.

[12] Ahmad, E.M., 2014. Photocatalytic, sonocatalytic and sonophotocatalytic degradation of rhodamine B using ZnO/CNTs composites photocatalysts. *Ultrasonics Sonochemistry*, 21, pp.761-773.

[13] Ahmad, M.M., 2002. Enhanced magnetization in sputter-deposited copper ferrite thin films. *Materials Science*, 246, pp.266-269.

[14] Mojahed, M., Dizaji, H.R., and Gholizadeh, A., 2022. Structural, magnetic, and dielectric properties of Ni/Zn co-substituted CuFe2O4 nanoparticles. *Physics B: Condensed Matter*, 646, p.414337.

[15] Rana, M.U., Islam, M., and Abbas, T., 2000. Cation distribution and magnetic interactions in Zn-substituted $CuFe_2O_4$ ferrites. *Materials Chemistry and Physics*, 65(3), pp.345-349.

[16] Ajmal, M., and Maqsood, A., 2008. Structural, electrical and magnetic properties of Cu1−xZnxFe2O4 ferrites ($0 \le x \le 1$). *Journal of Alloys and Compounds*, 460(1-2), pp.54-59.

[17] Adineh, Z., and Gholizadeh, A., 2021. Hydrothermal synthesis of Ce/Zr co-substituted $BiFeO_3$: R3c-to-P4mm phase transition and enhanced room temperature ferromagnetism. *Journal of Materials Science: Materials in Electronics*, 32, pp.26929-26943."

[18] Adineh, Z., and Gholizadeh, A., 2024. Comparison of sol-gel and hydrothermal synthesis methods on the physical, and photocatalytic properties of $Bi_{1-x}CexFe_{1-x}Al_xO_3$ ferrites. *Journal of Materials Science: Materials in Electronics*, 35, pp.745.

[19] Choupani, M., and Gholizadeh, A., 2021. The effect of calcination temperature on the X-ray peak broadening of t-CuFe2O4. *Progress in Physics of Applied Materials*, 1, pp.19.

[20] Gholizadeh, A., and Tajabor, N., 2010. Influence of N2- and Ar-ambient annealing on the physical properties of SnO2
transparent conducting films. *Materials Science in Semiconductor Processing*, 13, pp.162–166.

[21] Choupani, M., and Gholizadeh, A., 2024. Correlation between structural phase transition and physical properties of Co^{2+}/Gd^{3+} co-substituted copper ferrite. *Journal of Rare Earths*, 42, pp.1344-1353.

[22] Mojahed, M., Gholizadeh, A., and Dizaji, H.R., 2024. Influence of Ti4+ substitution on the structural, magnetic, and dielectric properties of Ni-Cu–Zn ferrite. *Journal of Materials Science: Materials in Electronics*, 35, pp.1239.

[23] Harish, V., Ansari, M.M., Tewari, D., Gaur, M., Yadav, A.B., García-Betancourt, M.L., Abdel-Haleem, F.M., Bechelany, M., and Barhoum, A., 2022. Nanoparticle and Nanostructure Synthesis and Controlled Growth Methods. *Nanomaterials (Basel)*, 12(18), pp.3226.

[24] Soleimani, F., Salehi, M., and Gholizadeh, A., 2017. Hydrothermal Synthesis, Structural and Catalytic Studies of CuBi2O4 Nanoparticles. *Journal of Nanoanalysis*, 4, pp.239-246.

[25] Gao, H., Wang, F., Wang, S., Wang, X., Yi, Z., and Yang, H., 2019. Photocatalytic activity tuning in a novel Ag2S/CQDs/CuBi2O4 composite: Synthesis and photocatalytic mechanism. *Materials Research Bulletin*, 115, pp.140-149.

[26] Soleimani, F., Salehi, M., and Gholizadeh, A., 2019. Comparison of visible light photocatalytic degradation of different pollutants by (Zn, Mg)xCu1-xBi2O4 nanoparticles. *Ceramics International*, 45, pp.8926–8939.

[27] Guo, F., Li, M., Ren, H., Huang, X., Hou, W., Wang, C., and Lu, C., 2019. Fabrication of pn CuBi2O4/MoS2 heterojunction with nanosheets-on-microrods structure for enhanced photocatalytic activity towards tetracycline degradation. *Applied Surface Science*, 491, pp.88-94.

[28] Esmaili, L., and Gholizadeh, A., 2020. The effect of Nd and Zr co-substitution on structural, magnetic and photocatalytic properties of Bi1-xNdxFe1-xZrxO3 nanoparticles. *Materials Science in Semiconductor Processing*, 118, p.105179.

[29] Beyranvand, M., Zahedi, A., and Gholizadeh, A., 2022. Cadmium substitution effect on microstructure and magnetic properties of Mg-Cu-Zn ferrites. *Frontiers in Materials*, 8, pp.779837